

## **Thermocapillary convection during hydrogen evolution at microelectrodes**

Massing, J.; Mutschke, G.; Baczyzmalski, D.; Hossain, S. S.; Yang, X.; Eckert, K.; Cierpka, C.;

Originally published:

December 2018

**Electrochimica Acta 297(2019), 929-940**

DOI: <https://doi.org/10.1016/j.electacta.2018.11.187>

Perma-Link to Publication Repository of HZDR:

<https://www.hzdr.de/publications/Publ-28536>

Release of the secondary publication  
on the basis of the German Copyright Law § 38 Section 4.

CC BY-NC-ND

# Thermocapillary convection during hydrogen evolution at microelectrodes<sup>☆</sup>

Julian Massing<sup>a,1,\*</sup>, Gerd Mutschke<sup>b,1,\*</sup>, Dominik Baczyzmalski<sup>a</sup>, Syed Sahil Hossain<sup>b</sup>, Xuegeng Yang<sup>b</sup>, Kerstin Eckert<sup>b,c</sup>, Christian Cierpka<sup>d</sup>

<sup>a</sup>*Institute of Fluid Mechanics and Aerodynamics, Universität der Bundeswehr München, D-85577 Neubiberg, Germany*

<sup>b</sup>*Helmholtz-Zentrum Dresden-Rossendorf (HZDR), 01314 Dresden, Germany*

<sup>c</sup>*Institute of Process Engineering, Technische Universität Dresden, D-01069 Dresden, Germany*

<sup>d</sup>*Institute of Thermodynamics and Fluid Mechanics, Technische Universität Ilmenau, 98684 Ilmenau, Germany*

---

## Abstract

The origin of strong electrolyte flow during water electrolysis is investigated, that arises at the interface between electrolyte and hydrogen bubbles evolving at microelectrodes. This Marangoni convection was unveiled only recently (X. Yang et al., PCCP, 2018, [1]) and is supposed to be driven by shear stress at the gas-liquid interface caused by thermal and concentration gradients. The present work firstly allows a quantification of the thermocapillary effect and discusses further contributions to the Marangoni convection which may arise also from the electrocapillary effect. Hydrogen gas bubbles were electrolytically generated at a horizontal Pt microelectrode in a 1 M H<sub>2</sub>SO<sub>4</sub> solution. Simultaneous measurements of the velocity and the temperature field of the electrolyte close to the bubble interface were performed by means of particle tracking velocimetry and luminescent lifetime imaging. Additionally, corresponding numerical simulations of the temperature distribution in the cell and the electrolyte flow resulting from thermocapillary stress only were performed. The results confirm significant Ohmic heating near the micro-electrode and a strong flow driven along the interface away from the microelectrode. The results further show an excellent match between simulation and experiment for both the velocity and the temperature field within the wedge-like electrolyte volume at the bubble foot close to the electrode, thus indicating the thermocapillary effect as the major driving mechanism of the convection. Further away from the microelectrode, but still below the bubble equator, however, quantitative differences be-

tween experiment and simulation appear in the velocity field, whereas the temperature gradient still matches well. Thus, additional effects must act on the interface, which are not yet included in the present simulation. The detailed discussion tends to rule out solution-based effects, generally referred to as solutal effects, whereas electrocapillary effects are likely to play a role. Finally, the thermocapillary effect is found to exert a force on the bubble which is retarding its departure from the electrode.

*Keywords:* water electrolysis, thermocapillary convection, microbubbles, fluorescence lifetime imaging, numerical simulation

---

## 1. Introduction

In the last decades, renewable energy technologies have become increasingly relevant due to the worldwide efforts to reduce CO<sub>2</sub> emissions. A major part of the future energy production in many countries will be based on wind and solar power. These volatile energy sources, however, cannot sustain a stable electrical grid and efficient energy storage and distribution systems are necessary. In light of these developments, hydrogen has attracted growing interest as an energy carrier for long-term storage, that can directly be produced through water electrolysis from the electricity provided by renewables. However, conventional alkaline water electrolyzers currently suffer from a relatively low efficiency, which limits their use on an industrial scale [3]. A significant contribution to the losses comes from hydrogen and oxygen gas bubbles forming at and sticking to the electrodes. On the one hand, they reduce the active electrode area, which causes higher electrode overpotentials and ultimately limits the hydrogen production rate. On the other hand,

---

<sup>☆</sup>Financial support from the AiF under the project No. 18941 N (JM) and from the DFG through the Emmy-Noether Research group program under grant No. CI 185/3 (DB and CC) is gratefully acknowledged. This work is further supported by the German Space Agency (DLR) with funds provided by the Federal Ministry of Economics and Technology (BMWi) due to an enactment of the German Bundestag under Grant No. DLR 50WM1758 (project MADAGAS).

\*Corresponding author

*Email addresses:* julian.massing@unibw.de (Julian Massing), g.mutschke@hzdr.de (Gerd Mutschke)

<sup>1</sup>These authors contributed equally to this work

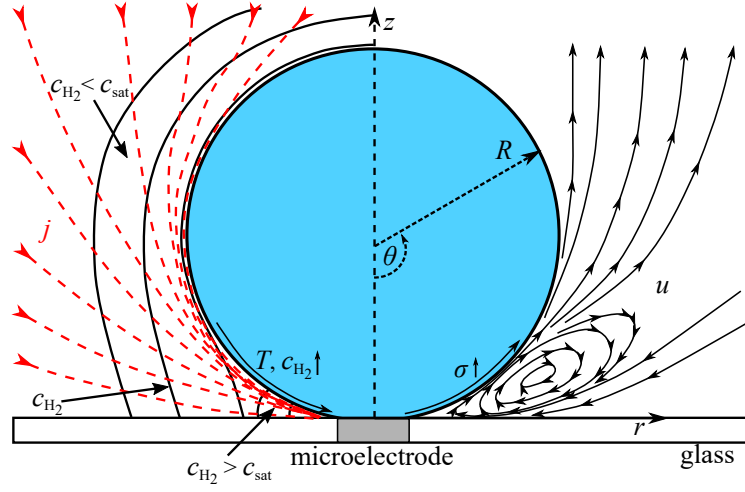


Figure 1: Sketch of the concentration of dissolved hydrogen  $c_{H_2}$  and the distribution of the current density  $j$  (left half, from [2]) and of the induced Marangoni flow near the hydrogen bubble (right half, from [1]). The axisymmetric coordinate system  $(r, z, \theta)$  where the symmetry axis passes the centers of hydrogen bubble and cathode (vertical dashed line) is defined as follows:  $r$  gives the radial distance to the symmetry axis,  $z$  measures the distance to the cathode surface, and the angle  $\theta$  is measured at the bubble center between the symmetry axis pointing downwards and the interface position, i.e. from bottom to top.

the bubbles reduce the effective electrical conductivity of the electrolyte, thus causing a higher ohmic resistance. In order to improve the efficiency of the process, several researchers have been studying different methods for accelerating the removal of gas bubbles from the electrodes [4, 5, 6, 7, 8, 9, 10, 11, 12, 13, 14, 15] or gaining improved understanding under microgravity condition [16, 17]. Nevertheless, a deeper understanding of the fundamental nucleation, growth and detachment mechanisms of single gas bubbles is still necessary. The investigation of individual gas bubbles at conventional electrodes, however, is nearly impossible due to the high bubble coverage and void fraction at practical current densities. For this reason, studies regarding single bubbles are often conducted at nano- or microelectrodes, which have the additional benefit that bubbles only grow within a small volume above the electrode surface, which is known at any given time. Therefore, they can be imaged more easily with high magnifications than on macroelectrodes where bubbles form at random positions on a larger surface [18, 19, 20, 21, 2, 1, 22]. Since electrolytic gas evolution occurs in many electrochemical systems, a better insight into this phenomenon is of high technical and scientific interest, not only for hydrogen production but also for a large number

of other industrial applications such as electrolyzers and photocatalytic reactors.

During electrolysis, gas bubbles are formed within the concentration boundary layer of the supersaturated gas at the electrode, known as the Nernst layer [23]. The detachment diameter of the bubble is dictated by the balance of the forces acting on the bubble. The buoyancy force and the pressure contact force tend to lift the bubble off the surface, whereas surface tension and often also hydrodynamic forces retard the bubble detachment [13]. In a recent experiment by Yang et al. [1], a strong electrolyte flow near hydrogen bubbles growing at a microelectrode was revealed which was attributed to be driven by a gradient of the surface tension  $\sigma$  along the interface of gas and electrolyte (see Fig. 1, right). Such types of flow are commonly referred to as Marangoni convection [24]. The resulting hydrodynamic force may delay the bubble detachment from the electrode, as recently reported by Chen et al. [25] for oxygen bubbles generated by photocatalysis. It is also well known, that Marangoni convection significantly influences the fluid dynamics and the mass transfer of rising bubbles or drops [26, 27, 28]. Furthermore, thermal Marangoni convection plays an important role for heat and mass transfer in subcooled pool boiling [29, 30, 31] where the flow is caused by a gradient of the local saturation temperature from top to bottom of the vapor bubble due to an accumulation of noncondensable gas at the bubble top, thereby decreasing the partial vapor pressure. Additionally, convection of the interface of mercury drops due to differences in the local interfacial potential caused by a non-uniform current distribution is known to be the source of polographic maxima of the first kind [32].

However, the origin of the Marangoni convection observed at hydrogen bubbles generated at microelectrodes during electrolysis is not yet clarified [1]. Generally, the shear stress boundary condition at the gas-liquid interface is given by:

$$\hat{\mathbf{t}} \cdot \boldsymbol{\tau}_{\mathbf{f}} \cdot \hat{\mathbf{n}} - \hat{\mathbf{t}} \cdot \boldsymbol{\tau}_{\mathbf{g}} \cdot \hat{\mathbf{n}} = \hat{\mathbf{t}} \cdot \nabla \sigma \quad (1)$$

where  $\hat{\mathbf{t}}$  and  $\hat{\mathbf{n}}$  denote the tangential and normal vector and  $\boldsymbol{\tau}_{\mathbf{f}}$  and  $\boldsymbol{\tau}_{\mathbf{g}}$  are the viscous stress tensors

of fluid and gas, respectively. Thus, a gradient of the surface tension generates an imbalance of the shear stress which causes the interface between fluid and gas to move. The resulting flow is directed from small to large values of surface tension (see Fig. 1, right). The gradient of the surface tension itself might be caused by thermal, solutal, voltaic and pressure effects [33]. When neglecting the small overpressure due to the Young-Laplace law inside large bubbles of diameter  $\sim 1$  mm, it reads:

$$\frac{\partial \sigma}{\partial s} = \gamma_1 \frac{\partial T}{\partial s} + \sum_i \gamma_2^{(i)} \frac{\partial c^{(i)}}{\partial s} + \gamma_3 \frac{\partial \Phi}{\partial s} \quad (2)$$

Here,  $s$ ,  $\gamma_1$ ,  $\gamma_2^{(i)}$  and  $\gamma_3$  denote the tangential coordinate along the interface and the partial derivatives of the surface tension with respect to temperature  $T$ , species concentration  $c^{(i)}$  and electric potential  $\Phi$ , respectively.

Thermal effects are related to the variation of the surface tension with temperature. At microelectrodes investigated here, a significant increase of the the current density  $j$  towards the wetted outer part of the electrode can be expected (see Fig. 1 left), and Ohmic heating  $\sim j^2/\sigma_{\text{el}}$ , where  $\sigma_{\text{el}}$  denotes the electrical conductivity of the electrolyte, will cause a temperature gradient along the interface.

Solutal effects are related to concentration gradients of surface active species, labeled by index  $i$ , i.e. ions or dissolved gases, along the interface. Especially due to the large current densities at microelectrodes, concentration variations of ions and related changes of pH are likely to occur near the bubble foot, but, to our knowledge, have not yet been studied in detail. Lubetkin [33] discussed the influence of the inhomogeneous concentration of the dissolved hydrogen in the Nernst layer as a possible mechanism, as depicted schematically in the left part of Fig. 1. However, it should be expected that thermodynamic equilibrium holds at the interface, which implies that the concentration of dissolved hydrogen will be equal to the saturation concentration defined by Henry's law. Thus, when neglecting the pressure and the temperature dependence of the Henry coefficient, a constant concentration of dissolved hydrogen along the interface is expected. Nevertheless, when

leaving the equilibrium argument aside, analysis revealed that due to strong oversaturation near the microelectrode, the solutal hydrogen effect could be of the same order as the thermal effect caused by Ohmic heating [1].

Besides this issue under discussion, the surface tension is also known to depend on voltaic effects (Lippman equation, [34, 35]), which might be of special importance here, where the bubble interface experiences a strongly inhomogeneous electric field near the microelectrode.

In order to clarify the contribution of the solutal, the thermal and the voltaic Marangoni effect at electrogenerated hydrogen bubbles growing at microelectrodes, it would be desirable to investigate the effects separately. However, in experiments always all effects are potentially present. Furthermore, simultaneous measurements of temperature, species concentration and electric potential at the interface of hydrogen bubble and electrolyte near the micro-electrode appear to be quite difficult. On the other hand, numerical modeling easily allows to selectively include single Marangoni effects into the simulations only.

In this work, the contribution of the thermocapillary effect to the Marangoni flow observed experimentally at hydrogen bubbles grown at micro-electrodes is studied in detail. The motivation is that the thermocapillary Marangoni effect is expected to be of major importance at microelectrodes. Therefore, the numerical modeling will be restricted to the thermal effect only. Simultaneous measurements of the temperature and the convection near the hydrogen bubble are performed, and the comparison with the numerical results allows to draw conclusions on the contribution of the thermocapillary effect to the Marangoni flow observed experimentally.

## **2. Numerics**

### *2.1. Simulation setup*

Numerical simulations are performed for a late stage of the bubble growth cycle ( $t/\tau_b = 0.8$ , with  $\tau_b$  denoting the duration of the bubble growth cycle) where the bubble growth rate  $dR/dt$  is small compared to the expected amplitude of the Marangoni convection. Thus, a bubble of fixed

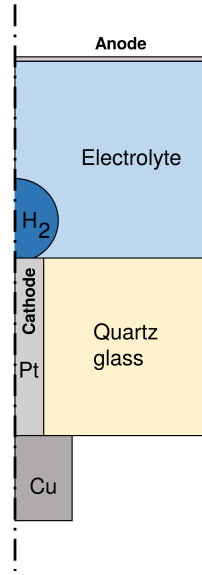


Figure 2: Sketch of the simulation setup in the  $(r,z)$ -plane. The dotted-dashed line denotes the symmetry axis  $r = 0$ . Length scales are modified for better visibility. Only an outer ring of the electrode of about  $9 \mu\text{m}$  in radial extension is wetted by the electrolyte, whereas the inner 67 % of the electrode surface are covered by the bubble.

size attached at the microelectrode is considered. The detailed geometrical data of the bubble and the corresponding value of the electrical current are taken from the experiment. The numerical setup slightly simplifies the more complex geometry of the electrochemical cell used in the experiment, as described below. The platinum cathode wire located at the center of the cuboid cell bottom has a radius of  $50 \mu\text{m}$  and a length of 5 mm. Because axial symmetry can be assumed in the region near the vertical center axis, a cylindrical cell is used, and 2D simulations are performed in the  $(r,z)$ -plane only. A sketch of the setup is shown in Fig. 2 where length scales were modified to clarify the geometric details near the hydrogen bubble. The vertical and the radial extension of the electrolyte volume is 5 mm. Here, the height is much smaller than in the experiment (45 mm) but is large enough to enable the local convection near the bubble interface to be simulated. The same argument applies for the upper electrode covering the electrolyte surface, which is far enough away to deliver a realistic distribution of the current density near the microelectrode. In the bottom part of the cell, a further simplification is applied, which is expected to reasonably model the important thermal fluxes out of the electrolyte volume, especially the large heat flux



through the cathode. Here, the thermal contact of the platinum wire to subsequent electrical metal connections is modeled by a single copper cylinder only, at which a proper boundary condition is applied (see below). The copper cylinder has a radius of 0.5 mm and a height of 1 mm, and the vertical extension of the bottom quartz glass part surrounding the cathode is 5 mm.

The electrochemical part of the problem is simplified to calculating the primary current density  $\vec{j}$  in the electrolyte from solving the Laplace equation for the electric potential  $\Phi$

$$\Delta\Phi = 0, \quad \vec{j} = \sigma_{\text{el}} \nabla\Phi. \quad (3)$$

For the aqueous electrolyte containing 1M  $\text{H}_2\text{SO}_4$ , a constant electrical conductivity of  $\sigma_{\text{el}} = 40 \text{ S/m}$  is assumed. A constant voltage is applied at the electrodes such that the Faradaic current of the cell amounts to 2.95 mA, in accordance to the depicted instant of the bubble cycle (see Fig. 6).

The temperature distribution  $T(r, z, t)$  is calculated from solving the coupled equations of convective heat transfer in the domains of the electrolyte, the  $\text{H}_2$  bubble, the Pt wire and the glass at the bottom of the cell.

$$\rho c_p \left( \frac{\partial T}{\partial t} + \vec{u} \cdot \nabla T \right) = k \Delta T + \frac{j^2}{\sigma_{\text{el}}} \quad (4)$$

Here,  $\rho$ ,  $c_p$ ,  $k = D_{\text{th}} \rho c_p$ ,  $D_{\text{th}}$  and  $\vec{u}$  denote the corresponding material parameters density, heat capacity, thermal conductivity, thermal diffusivity and the advection velocity (nonzero only inside the electrolyte), respectively. The simulation takes into account the dominant Ohmic heat source of  $Q = j^2 / \sigma_{\text{el}}$  in the electrolyte only. At the bottom of the quartz glass and at the bottom of the copper wire, an ambient temperature of  $T_0 = 20 \text{ }^\circ\text{C}$  is set, whereas at the remaining outer boundaries and at the top of the cell thermal insulation applies. At material interfaces, continuity of temperature is assumed. The material parameters used in the simulation are:

platinum:  $\rho = 21450 \text{ kg/m}^3$ ,  $c_p = 130 \text{ J/(kg} \cdot \text{K)}$ ,  $k = 72 \text{ W/(m} \cdot \text{K)}$ ;  
 copper:  $\rho = 8700 \text{ kg/m}^3$ ,  $c_p = 385 \text{ J/(kg} \cdot \text{K)}$ ,  $k = 400 \text{ W/(m} \cdot \text{K)}$ ;  
 electrolyte:  $\rho = 1000 \text{ kg/m}^3$ ,  $c_p = 4182 \text{ J/(kg} \cdot \text{K)}$ ,  $k = 0.58 \text{ W/(m} \cdot \text{K)}$ ;  
 hydrogen:  $\rho = 0.09 \text{ kg/m}^3$ ,  $c_p = 14320 \text{ J/(kg} \cdot \text{K)}$ ,  $k = 0.186 \text{ W/(m} \cdot \text{K)}$ ;  
 quartz glass:  $\rho = 2201 \text{ kg/m}^3$ ,  $c_p = 1052 \text{ J/(kg} \cdot \text{K)}$ ,  $k = 1.38 \text{ W/(m} \cdot \text{K)}$ .

The transient Navier-Stokes equation is solved for the electrolyte only and takes into account buoyancy due to change of temperature within the Boussinesq approximation:

$$\rho \left( \frac{\partial \vec{u}}{\partial t} + \vec{u} \cdot \nabla \vec{u} \right) = -\nabla p + \eta \Delta \vec{u} - \rho \beta \vec{g} (T - T_0) \quad (5)$$

Here,  $\rho_0$ ,  $\eta$ ,  $\beta$ ,  $p$  and  $\vec{g}$  denote the density, the viscosity and the coefficient of thermal expansion of the electrolyte, the pressure and the downward directed vector of gravitational acceleration, respectively. At the interface between hydrogen bubble and electrolyte, the normal velocity component has to vanish, and the thermal Marangoni condition (1) holds whereby the tangential stress at the bubble side is neglected due to the much lower viscosity of the gas. At all other boundaries, a non-slip condition is applied. The following material parameters were used:  $\beta = 3 \cdot 10^{-4} \text{ K}^{-1}$ ,  $\eta = 1 \cdot 10^{-3} \text{ kg/(m} \cdot \text{s)}$ . For the Marangoni condition, the surface tension and the temperature coefficient were set to that of a water-air system as  $\sigma_0 = 0.072 \text{ N/m}$ ,  $\gamma_1 = -1.6 \cdot 10^{-4} \text{ N/(m} \cdot \text{K)}$ . Transient simulations were performed starting at ambient temperature from an electrolyte at rest with constant Faradaic current for a period of 6 s at maximum to investigate the temporal evolution of the cell temperature and the convection inside the electrolyte.

## 2.2. Simulation Methodology

The late stage of the bubble evolution for which simulations were performed is marked gray in Fig. 6. Here, the bubble growth rate can be estimated to  $dR/dt \approx 83 \text{ } \mu\text{m/s}$ , which is more than two orders of magnitude smaller than the amplitude of the observed Marangoni convection,

thus justifying the approach of using a fixed bubble size in the simulations. According to the experiment, the size of the spherical bubble is assumed to be  $R = 560 \mu\text{m}$ , and the center of the bubble is located  $R - 1.5 \mu\text{m}$  above the center of the cathode, such that the largest part of the cathode is covered by the bubble, and only an outer ring of about  $9 \mu\text{m}$  in radial extension remains wetted (see Fig. 2). The resulting contact angle measured from the bubble center between the symmetry axis pointing downward and the bubble interface position at the cathode amounts to  $\theta_c \approx 4.2^\circ$ .

Next the different time scales involved are discussed. The bubble cycle  $\tau_b$  in physical units amounts to about 4.1 s, whereas the sampling period of the velocity and temperature measurement according to Fig. 6 is about 0.4 s only. In the transient simulations, which start from ambient temperature  $T_0$  when the cell current is switched on, the characteristic time of thermal diffusion in the electrolyte amounts to  $\tau_{\text{th}} = R^2 \rho c_p / k \approx 2.2 \text{ s}$ , whereas in the hydrogen bubble it is only  $\tau_{\text{th}} \approx 2.2 \text{ ms}$ . However, heat is also advected by the thermocapillary motion of the electrolyte that is forced immediately at the interface. When considering the Peclet number ( $Pe$ ) which describes the ratio of convective to diffusive heat transfer, by assuming a characteristic velocity  $U$  of 10 mm/s, a characteristic length being equal to the bubble radius  $R$  and the thermal diffusivity  $D_{\text{th}} = k/(\rho c_p)$  of the electrolyte given above,  $Pe = UR/D_{\text{th}} \sim 40$  is obtained, stating that convective transport clearly dominates. It can therefore be expected that the temperature and the velocity profile near the interface develop rather quickly within less than a second. On the other hand, the thermocapillary motion driven at the interface is expected to create a vortical flow within the  $(r, z)$ -plane, as sketched in Fig. 1, right. Therefore, in order to account for realistic values also more far away from the bubble interface, the characteristic time scale of the eddy circulation should be considered. When approximating the eddy shape by a circle of the size of the hydrogen bubble, by assuming a characteristic velocity of 10 mm/s, an eddy recirculation time of only about  $2\pi \cdot R/U \sim 0.35 \text{ s}$  is obtained.

As mentioned above, inside the hydrogen bubble diffusion of heat is taken into account whereas

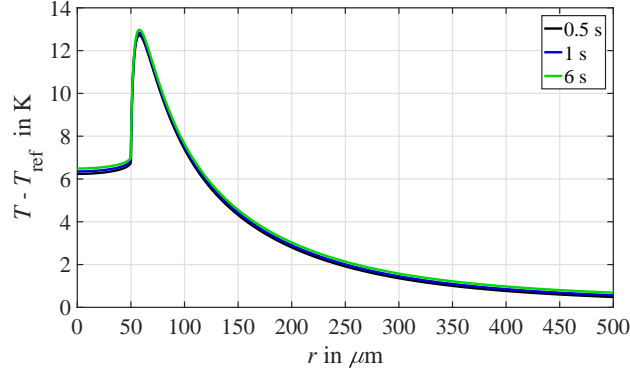


Figure 3: Temperature vs. radial coordinate  $r$  along the cathode and the bottom wall of the cell at different instants of time from the transient simulation.

convective heat transport is neglected. When using a characteristic velocity  $U$  of 10 mm/s, a characteristic length being equal to the bubble radius  $R$ , and the thermal diffusivity of hydrogen given above, a small Peclet number of only about  $Pe \sim 0.1$  is obtained, which justifies the approximation made.

Finally, it is mentioned that the time scale of diffusive heat transfer through the glass bottom based on the glass height is slow and amounts to about 42 s, thus also the temperature at the bottom is determined mainly by the advective time scale, which becomes also visible from the simulation result shown in Fig. 3.

In summary, the above estimations show that when switching on the electrical current, within a period of less than 1 s nearly stationary temperature and velocity fields near the bubble interface will develop, which can be expected to realistically model the experimental data depicted for the late instant of the bubble cycle. In the following the results of the transient simulation at  $t = 1$  s are used for comparison with the experimental data. The simulations were performed with COMSOL Multiphysics, version 5.3.

### 3. Experiment

#### 3.1. Electrochemical setup

The electrochemical setup was equivalent to that used by Yang et al. [1]. Water electrolysis was carried out within a glass cuvette with a three-electrode system under potentiostatic conditions [2] (see Fig. 4). As the working electrode a platinum wire with a diameter of  $100\ \mu\text{m}$  was used. The wire was embedded in a glass tube with an outer diameter of 6 mm, which formed the bottom of the electrolysis cell. A 1 M  $\text{H}_2\text{SO}_4$  solution served as the electrolyte. All electrode potentials refer to mercury/mercurous sulphate electrode (MSE, 650 mV vs. standard hydrogen electrode (SHE)). A potential of -7 V was applied to the working electrode, which enables the production of relatively large bubbles ( $\sim 1\ \text{mm}$ ) without any electrochemical side reactions. As the larger bubble size gives rise to larger flow structures, accurate measurements of the Marangoni convection and the temperature field at the foot of the growing bubble become feasible. To avoid continuous heating of the bulk electrolyte the potential was only applied over a short time period of 30 s. During this electrolysis cycle 7 bubbles were produced. Since phase averaging over a large number of bubbles was necessary for a high measurement resolution, as will be discussed later, 100 electrolysis cycles were run which resulted in a total number of approx. 700 single bubbles for this experiment. During the experiment, the bulk temperature of the electrolyte, in the following denoted as  $T_{\text{ref}}$ , was continuously measured with a Pt100 resistance thermometer. No heating of the electrolyte was observed, and therefore  $T_{\text{ref}}$  equals the room temperature.

#### 3.2. Measurement Methodology

Fig. 4 schematically depicts the measurement setup. A high speed camera (PCO DIMAX HS4 by PCO GmbH) equipped with a Zeiss EC Plan-Neofluar  $10\times/0.3$  microscope objective lens was used to visualize the growing bubble and to measure the temperature and velocity field around it, resulting in a field of view of approx.  $1 \times 1\ \text{mm}^2$ . Temperature sensitive luminescent tracer

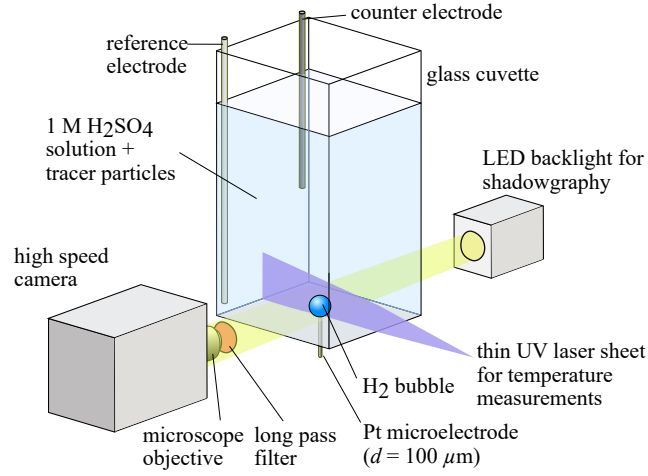


Figure 4: Experimental setup.

particles were added to the electrolyte to obtain the temperature and velocity field simultaneously. These particles consist of a polymethylmethacrylate (PMMA) matrix that is doped with the two luminescence dyes europium thenoyltrifluoroacetate (EuTTa) and perylene [36]. The particles are monodisperse with a mean particle diameter of  $7\ \mu\text{m}$ . To illuminate the particles in the center plane of the bubble a thin laser sheet generated by a 355 nm double pulse Nd:YAG laser was used (see Fig. 4). When excited at this wavelength, the EuTTa dye emits phosphorescent light in the red wavelength range, whereas the perylene dye emits blue fluorescence. The temperature measurement principle is based on the fact that the initial intensity and the luminescence lifetime of the EuTTa signal depend on temperature, while the perylene signal is temperature insensitive. As in two-color laser induced fluorescence (LIF) [37] the temperature insensitive dye serves as a reference to correct for spatial or temporal variations in the illumination intensity. In the present case, however, a luminescence lifetime based technique was applied to measure the temperature via the signals of individual particles [38, 39]. Since the lifetime is an intrinsic property of the appropriated dye, it is not affected by variations in the illumination intensity, variations in the dye concentration or photobleaching and no additional reference signal is needed. Thus, only the red part of the luminescent light is of interest here and the blue part was filtered out by a 570 nm long pass filter placed in front of the microscope objective.

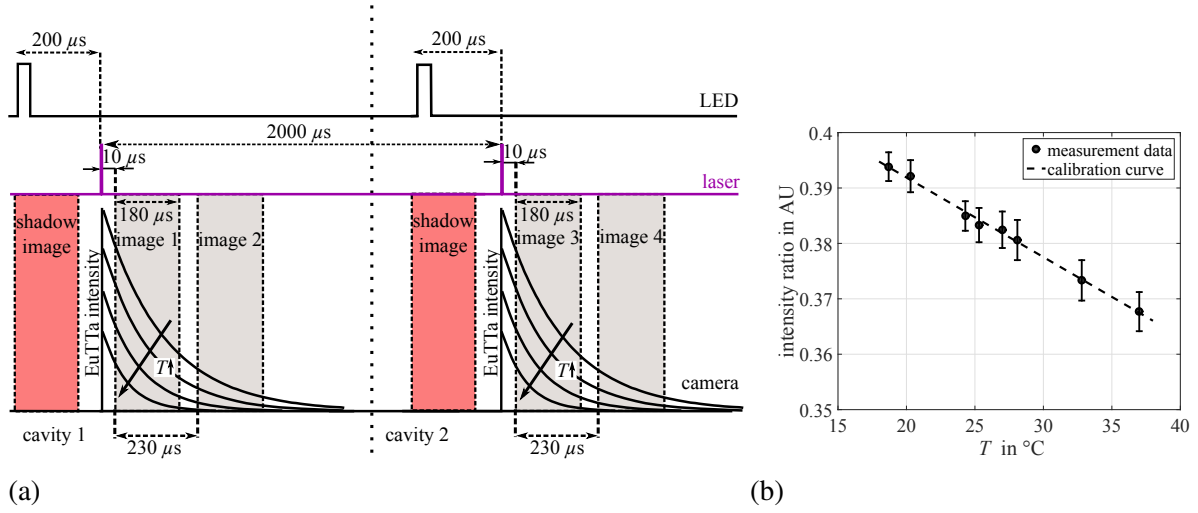


Figure 5: a) Timing sequence for temperature measurements and b) Calibration curve for temperature measurements.

After each laser pulse, the excited EuTTa luminescence decays exponentially over a time period in the order of several hundred  $\mu\text{s}$ , as sketched in Fig. 5a. During the decay, two images are taken in short succession by the high speed camera. The lifetime of the luminescence, which is defined as the time when the intensity has decayed to  $1/e$  of its initial value, decreases with increasing temperature. Consequently, the ratio of the mean particle image intensity in the second and first image similarly decreases with increasing temperature. Using a proper calibration procedure, the intensity ratio of each particle image can be directly related to the particle's temperature. However, an *in situ* temperature calibration was not possible with the present experimental setup and an *ex situ* calibration had to be performed. For this reason, a correction function depending on the luminescent intensity in the first image was applied to account for the non-linear response of the camera sensor, similar to the approach of Zhou et al.[40].

In addition to the flow and temperature field, the bubble geometry was visualized via shadowgraphy. As sketched in Fig. 4, a white LED background illumination was used to obtain bubble shadow images. The timing sequence used for the camera recordings and the two light sources is illustrated in Fig. 5a. In general, three images were recorded per laser pulse at approx. 4350 fps. The first image in this sequence was triggered prior to the laser pulse together with the LED

background illumination in order to record a bubble shadow image. Note that the blue part of the LED spectrum was removed by an additional filter to avoid excitation of the particle luminescence during the shadow image. The next two images were taken shortly after the laser pulse to determine the temperature from the luminescence decay. The short time delay of  $10\ \mu\text{s}$  between the laser pulse and the first luminescence image was chosen to avoid laser light reflections from the bubble in this image. This is necessary since the long pass filter in front of the microscope objective does not perfectly block the laser light. The resulting calibration curve is depicted in Fig. 5b. The uncertainty of the temperature measurement, estimated based on the calibration data, is approx.  $\pm 2.2\ \text{K}$  for individual particle images (standard deviation). However, the accuracy can be considerably increased since phase-resolved ensemble averaging is applied, as will be explained later. Furthermore, since a gradient of the pH-value can be expected at the bubble foot, it should be also mentioned that no pH-sensitivity of the luminescence lifetime was found in a separate test investigating different solutions in the range of  $0 \leq \text{pH} \leq 4$ .

The flow velocity was measured by particle tracking velocimetry (PTV) using two luminescent particle image pairs. However, using the two consecutive lifetime images for tracking leads to high relative uncertainties, since the particle displacement between those images was less than 1 pixel. Instead, the images recorded after the first and second laser pulse were used (denoted as image 1 and image 3 in Fig. 5). The time distance between these images, i.e. the pulse distance,  $\Delta t = 2000\ \mu\text{s}$ , was set to enable accurate measurements of the fast Marangoni convection at the gas-liquid interface.

Since the laser sheet is about  $500\ \mu\text{m}$  thick, out-of-focus particles may also contribute to the image, although with a much lower intensity than in-focus particles. However, to avoid the influence of such out-of-focus particles on the temperature measurements, only a very low tracer particle concentration was used. Therefore, a simple nearest neighbor tracking approach could be applied for the PTV evaluation [41]. Despite the low particle concentration, temperature and velocity fields with a high spatial resolution can be obtained by phase-averaging the data mea-



sured for a large number of growing bubbles. This was possible since the bubble evolution cycle is highly periodic, as shown in previous studies [21, 13, 12, 19]. For this purpose, the bubble evolution cycle was divided into 10 phases. The bubble size, which was obtained from the shadow images, served to receive the phase information. After sorting the data according to its phase, the spatial temperature distribution was determined by averaging the data in bins of  $12 \times 12 \text{ pixel}^2$  ( $15.3 \times 15.3 \mu\text{m}^2$ ). For the velocity data, a bin size of  $6 \times 6 \text{ pixel}^2$  ( $7.7 \times 7.7 \mu\text{m}^2$ ) was applied.

## 4. Results

### 4.1. Bubble dynamics

The evolution of the bubble diameter and of the electric current during one bubble growth cycle are depicted in Fig. 6 for a cathodic potential of -7 V. A more detailed discussion of the typical behavior of the current at a microelectrode during a bubble cycle can be found in [21]. At the beginning of the cycle, the current magnitude reaches a peak since the diameter of the newly formed bubble and thus the electrode coverage is small. With increasing bubble diameter a growing part of the electrode gets blocked, which leads to an only slowly increasing current magnitude over almost 80 % of the bubble lifetime. During this phase the bubble diameter follows the  $d_b(t) \propto t^{1/3}$  relation, which is typical for high current densities at the surface, particularly for microelectrodes [19, 21, 42]. Because of the high local supersaturation level in this regime, almost the entire hydrogen generated at the electrode surface diffuses directly into the bubble at its foot. In the late phase, the bubble diameters deviate from this law in form of an accelerated growth due to a strong increase of the magnitude of the cathodic current. The bubble detaches from the surface approx. 4 seconds after nucleation with a diameter of approx. 1.3 mm. At this point the buoyancy exceeds the forces that retard bubble detachment. Immediately after the bubble detaches a new bubble is formed at the electrode and the process is repeated. The addition of tracer particles does not alter the bubble dynamics as was shown in previous experiments [1]. As already mentioned, the bubble growth cycle is highly periodic [21, 13, 12, 19, 1] which enables

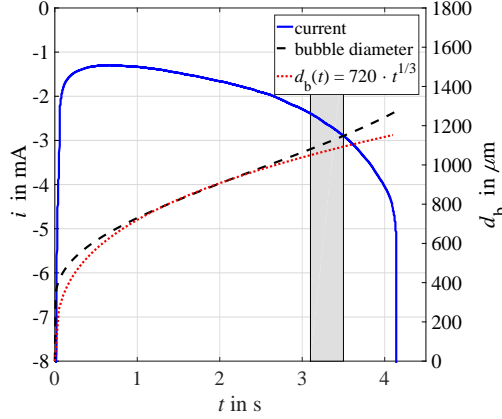


Figure 6: Evolution of the electric current and of the bubble diameter during one bubble growth cycle. The grey range marks the sampling period (see text).

phase averaging over multiple bubbles. The gray area in Fig. 6 depicts the time period that was used for phase averaging ( $0.75 \lesssim t/\tau_b \lesssim 0.85$ ). A later state of the bubble growth cycle was chosen, since the bubble diameter and thus the flow structures are relatively large and the bubble growth is relatively slow, which enables accurate measurements of the temperature and velocity field with a high spatial resolution.

#### 4.2. Marangoni effect

Ohmic losses lead to significant heating of the electrolyte especially near the microelectrode where the spatial current density is at its maximum. Furthermore, heat conduction in the surroundings influences the temperature distribution. Fig. 7 shows a zoomed view of the temperature distribution  $T - T_{\text{ref}}$  near the bubble foot from the simulation. Maximum heating occurs in the small wedge between bubble and cell bottom/electrode near the outer edge of the cathode where the current density is expected to be largest. The pear-like shape of the heated region visualizes the downward diffusion of heat inside the cathode wire.

Fig. 8a depicts in a closer view the numerically simulated (left) and the experimentally measured (right) temperature field of the electrolyte in the vicinity of the hydrogen bubble. A good qualitative and quantitative match between both can clearly be seen. As already mentioned, due

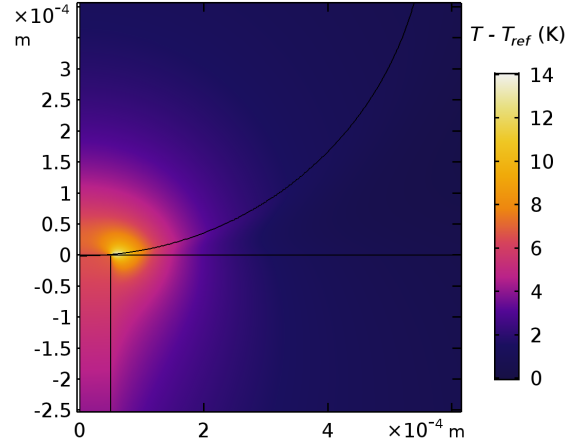
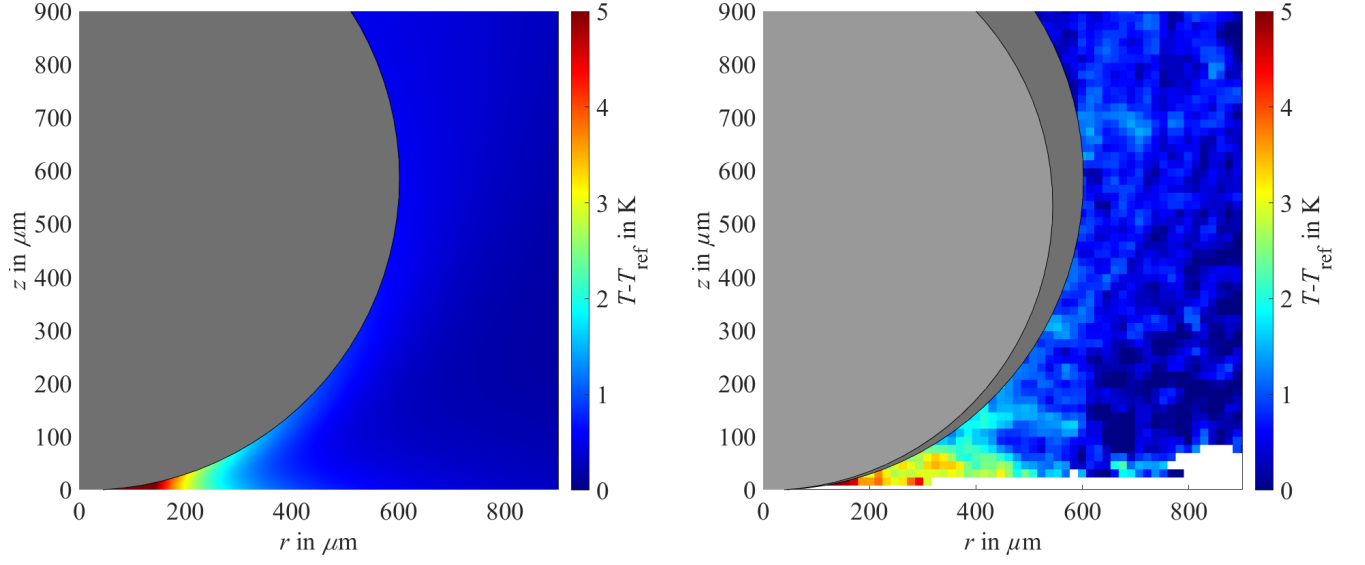


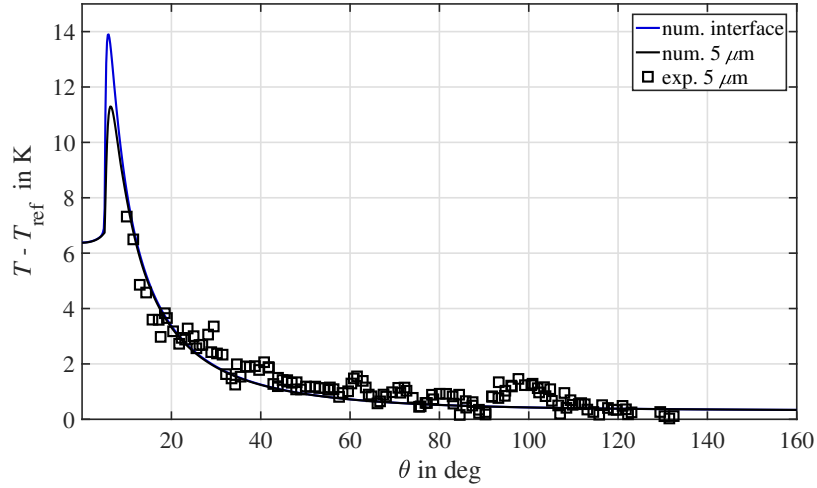
Figure 7: Temperature of gas, electrolyte and cell from the simulation in the  $(r, z)$ -plane. Zoomed view near the bubble foot. The geometry edges are marked as black lines.

to the high current density, the electrolyte significantly heats up near the bubble foot. From the simulation data along the gas-liquid interface in Fig. 8b, a maximum temperature rise of approx. 14 K is found approximately above the outer edge of the microelectrode where the current density is highest. In the experiment, a similar temperature increase towards the bubble foot is observed. However, the temperature directly at the contact between bubble and electrode could not be measured due to shadowing effects and reflections at the bottom wall of the cell. Nevertheless, from Fig. 8b a very good match of the temperature distribution along the interface between experiment and simulation becomes evident. Here, because of the finite size of the tracer particles, a normal distance of about  $5 \mu\text{m}$  away from the interface was chosen for detailed comparison with the experiment. With increasing  $\theta$  beyond the temperature maximum at about  $\theta \approx 7^\circ$ , an exponential-like decay of the temperature difference is observed, with a steep gradient in the beginning. At  $\theta \approx 30^\circ$ , the gradient has already decreased to about  $0.04 \text{ K}/\mu\text{m}$ , and for  $\theta \geq 110^\circ$  the temperature remains nearly constant.

In Fig. 9a the numerically calculated Marangoni convection, which is solely driven by the temperature gradient, is compared with the Marangoni convection measured during electrolysis. Both results show in qualitative agreement a strong flow at the electrode-near part of the gas-



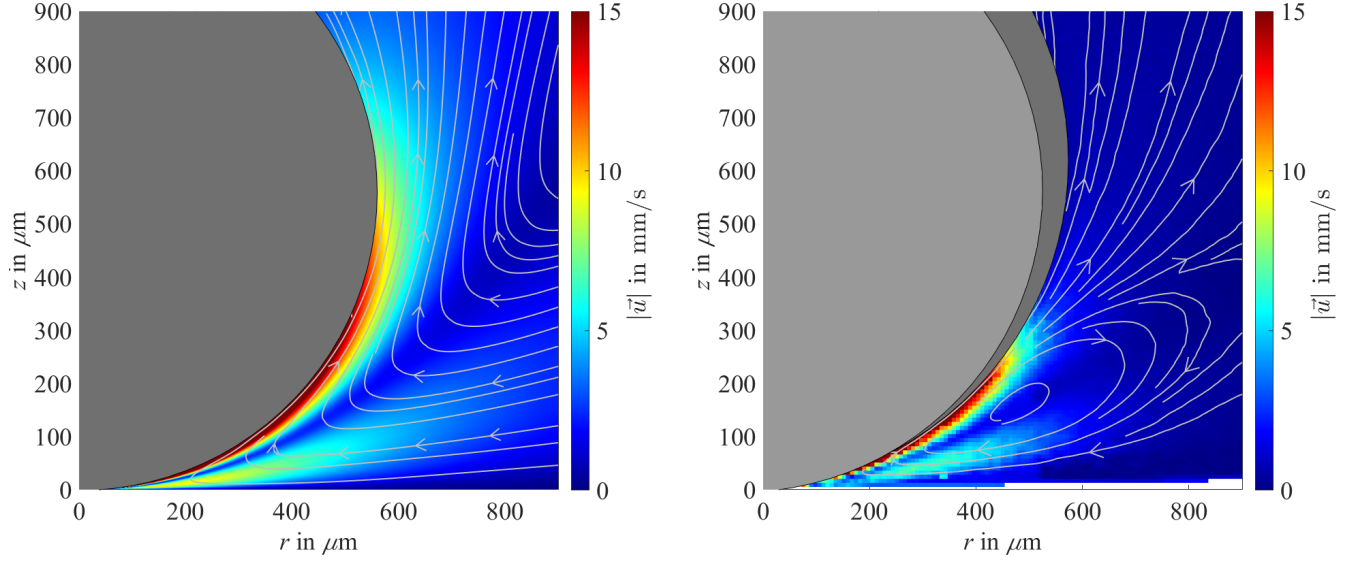
(a)



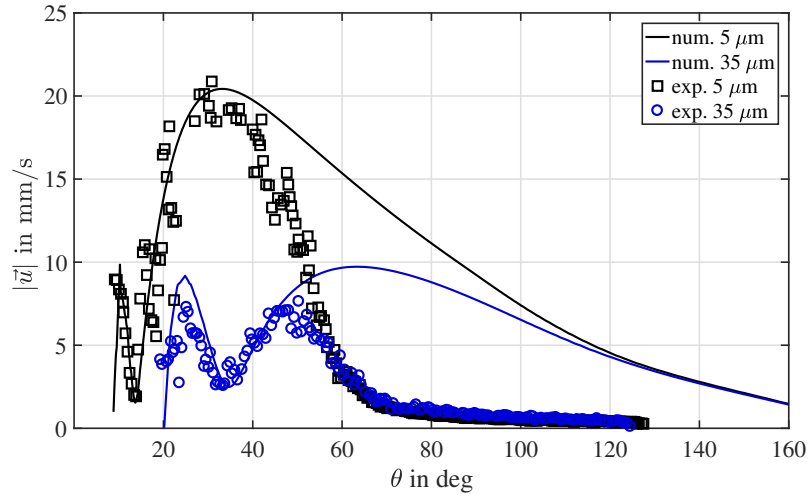
(b)

Figure 8: (a): Temperature of the electrolyte near the bubble interface. Left: simulation, right: measurement. The maximum of the color bar is limited by hand to 5 K to facilitate comparison. (b): Temperature at and in  $5\ \mu\text{m}$  distance along the interface. The angle  $\theta$  is measured from bottom to top, as defined in Fig. 1.

liquid interface, from which it can already be concluded that a substantial part of the measured Marangoni convection is caused by the thermocapillary effect. However, a more detailed analysis reveals that in the numerical case the accelerated region near the interface reaches the bubble equator and is thus more extended compared to the experiment where the velocity decays more quickly with increasing  $\theta$ . From the simulation results that, despite not shown in number, the



(a)



(b)

Figure 9: (a): Marangoni convection  $|\vec{u}|$  in the electrolyte near the bubble interface. Left - numerical simulation of the thermal Marangoni effect. Right - measurement of the Marangoni convection during electrolysis. The color bar is limited by hand to 15 mm/s to facilitate comparison. (b): Comparison of the electrolyte convection  $|\vec{u}|$  along the interface. Simulation and measurement results at normal distances of  $5 \mu\text{m}$  and  $35 \mu\text{m}$  away from the interface. The angle  $\theta$  is measured from bottom to top, as defined in Fig. 1.

convection which is forced directly at and parallel to the gas-liquid interface reaches a maximum velocity of  $u \approx 30 \text{ mm/s}$ . Normal to the interface, the velocity quickly decays. Because of mass conservation, the interface-parallel removal of electrolyte from the bubble-foot region leads to a nearly horizontal replenishment flow, and a vortex forms, as shown in Fig. 9a. In the experiment,

the vortex center is located close to the bubble foot. This observation of Marangoni convection coincides with results of similar measurements from Yang et al. [1] (see Fig. 1). In the simulation, however, as the accelerated region along the interface is larger, the vortex center is located further away from the bubble foot.

Fig. 9b investigates in detail the behavior of the velocity magnitude along the interface. Again, because of the finite size of the tracer particles, a curve at  $5\ \mu\text{m}$  distance and a second curve at  $35\ \mu\text{m}$  distance away from the interface are depicted for comparison of experimental and numerical results. Within the wedge-like electrolyte volume at the bubble foot, the velocities agree very well in both cases. The first velocity peak at  $\theta \approx 10^\circ$  ( $5\ \mu\text{m}$ ) and respectively  $\theta \approx 25^\circ$  ( $35\ \mu\text{m}$ ) is attributed to the flow close to the bottom wall directed towards the bubble foot, which replenishes the displaced electrolyte. At the first peak, the measured velocity magnitude at  $5\ \mu\text{m}$  away from the interface is approx.  $1\ \text{mm/s}$  smaller than in the simulation, whereas at  $35\ \mu\text{m}$  it is  $2\ \text{mm/s}$  smaller. However, this difference can be explained by the averaging imposed by the spatial binning. The experimental data represents the mean velocity in each bin. Since the velocity gradient is very steep, the velocity peak is biased to smaller values due to the spatial averaging [43]. Continuing along the interface, the experimental and numerical data keep on to coincide very well up to  $\theta \approx 40^\circ$  for the case close to the interface and up to  $\theta \approx 50^\circ$  at a distance of  $35\ \mu\text{m}$ .

At the interface distance of  $5\ \mu\text{m}$ , in good agreement of simulation and experiment, the largest velocity of about  $20.5\ \text{mm/s}$  is found at a second local maximum at  $\theta \approx 30^\circ$ . Further upward along the interface, the measured velocity starts to sharply decrease, whereas the simulated value of the velocity, is decaying more slowly. At a distance of  $35\ \mu\text{m}$  away from the interface, the simulation yields a maximum of about  $u = 9.8\ \text{mm/s}$  at  $\theta = 65^\circ$  whereas the velocity maximum found in the experiment is of only about  $7.1\ \text{mm/s}$  at an angle of about  $\theta = 50^\circ$ . This difference can be attributed to the different position of the recirculating vortex discussed above. Again, when moving on along the interface, the experimental velocity decays much faster than the simulated one. From the experimental data it can be seen that the velocity in both discussed cases falls

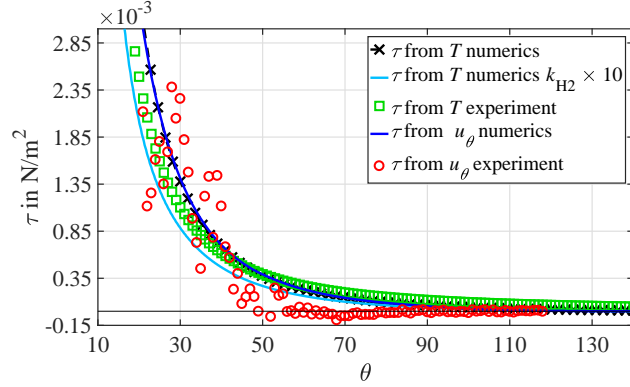


Figure 10: Comparison of the shear stress  $\tau$  originating from different sources along the bubble interface.

below 1 mm/s at  $\theta \approx 75^\circ$  and reaches zero at  $\theta \approx 120^\circ$ . In comparison, the decay of velocity in the simulation is clearly less steep, which coincides with the larger extent of the accelerated interface region discussed in Fig. 9a.

## 5. Discussion

The numerical and experimental data show a very good agreement within the wedge-like electrolyte volume at the bubble foot for both the temperature and the velocity. The high current density close to the electrode leads to a significant temperature increase with a strong gradient, which could be predicted well by the numerical model. The temperature gradient drives a fast Marangoni convection, as can be seen from the simulation which only takes the thermo-capillary effect into account. Close to the bubble foot, the experimentally determined velocities agree very well with the numerically calculated values. Thus, it can be concluded that the thermal effect is in fact the major driving mechanism for the Marangoni convection observed in this experiment and by Yang et al. [1]. If a solutal Marangoni effect exists, it only plays a minor role in this configuration. However, the extension of the Marangoni-accelerated interface is clearly over-predicted by the simulation. The fluid decelerates much faster in the experiment than in the simulation to become almost stagnant near the bubble equator.

The thermal Marangoni balance (1) at the interface between bubble and electrolyte can be sim-

plified by neglecting the hydrogen shear part. As the interface-normal component of the velocity must vanish, it reads [44]:

$$\tau = \eta r \frac{\partial}{\partial r} \left( \frac{u_\theta}{r} \right) = \frac{1}{r} \frac{d\sigma(T)}{d\theta} \quad (6)$$

Here, axial symmetry is assumed, and spherical coordinates where used. This equality allows for the comparison of the shear stress  $\tau$  originating from different sources, based on the interface-normal gradient of the tangential velocity  $u_\theta$  and on the tangential gradient of the surface tension. As a linear dependency of the surface tension on temperature given by the Eötvös rule  $\sigma(T) = \sigma_0 - \gamma_1 \cdot (T - T_{ref})$  is assumed, its gradient can be determined from the temperature data.

For the experiment, the interface-normal velocity gradient  $(\frac{\partial}{\partial r} (\frac{u_\theta}{r}))$  along the interface was determined from a linear fit of the velocity data which are closest to the interface. The results obtained are shown in detail in Fig. 10. For the simulation results, as expected from the Marangoni boundary condition (eq. (1)) applied, the shear stress calculated from the temperature distribution (black x symbols) perfectly matches the calculated velocity gradient (blue line). In comparison, the experimental result of the shear stress calculated from the temperature distribution measured (green square symbols) shows a rather close match with the numerics, with slightly smaller values at small angles  $\theta < 48^\circ$  and slightly larger values further along. However, looking at the shear stress calculated from the velocity data measured (red circle symbols), larger differences to the numerical data are found. Despite the fact that the scatter of data at small angles does not allow a quantitative comparison, it is clearly seen that at larger angles  $\theta > 35^\circ$  the shear stress is falling much more rapidly to zero when compared to the numerical result. This result coincides with the match of the temperature distribution along the interface and the mismatch of the velocity distribution arising at larger distances away from the microelectrode as discussed at Figs. 8 and 9. It further underlines the reasoning that other phenomena beyond the thermocapillary effect must exist which are not yet implemented in the numerical model. These counteract the thermocapillary effect in the upper part of the bubble and decelerate the Marangoni convection, which is likely also



to influence the position of the center of the recirculation region, as discussed above.

The Marangoni flow driven at the interface leads to a force on the bubble, which adds to the force balance and thus influences the instant of departure and the dynamics of the bubble. Integration of the shear stress given in eq. (6) over the bubble interface

$$F_M = - \int \tau dA \quad (7)$$

yields a resultant force in vertical direction (Fig 1). Hereby,  $dA$  denotes the interface-normal area differential, and according to eq. (2) it holds

$$\frac{\partial \sigma}{\partial \theta} = \gamma_1 \frac{\partial T}{\partial \theta} \quad (8)$$

The calculated Marangoni force on the bubble amounts to  $0.79 \mu\text{N}$  and is directed downward, thus retarding the departure of the bubble from the electrode. In comparison, the buoyancy force acting on this bubble of  $0.56 \text{ mm}$  radius is  $7.2 \mu\text{N}$  in the upward direction. Therefore, the modulus of the Marangoni force is one order of magnitude weaker than the buoyancy force.

In the following, possible further aspects neglected in the simulations so far are discussed. Overall, it has to be kept in mind that in this work results of a transient simulation of electrolysis near a hydrogen bubble of fixed size attached at a microelectrode are compared with experimental phase-averaged results from the periodic growth of hydrogen bubbles. For the late stage of the bubble cycle depicted, it can be assumed that the convection related to the lift-off of the previous bubble has already declined [21]. Furthermore, as estimated above, the magnitude of flow caused by the growth of gas volume is small compared to the Marangoni convection. The instant of time ( $t = 1 \text{ s}$ ) depicted for presenting the simulation results was derived from an order of magnitude estimation. Fig. 11 depicts the transient behavior of the velocity magnitude  $5 \mu\text{m}$  away from the bubble interface at  $\theta = 33^\circ$  where the maximum velocity was found (see Fig. 9). As can be seen, already after  $0.1 \text{ s}$  the interface is moving almost with its final speed, which gives further support

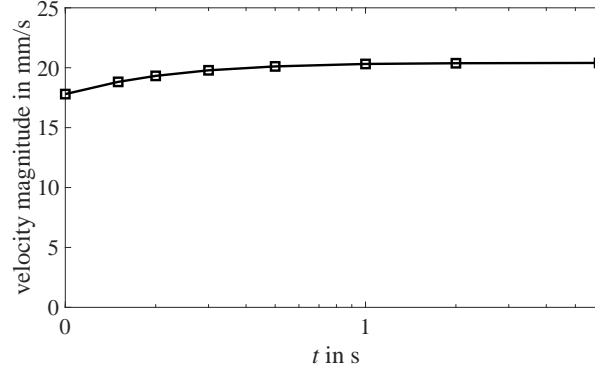


Figure 11: Simulation of the temporal behavior of the velocity magnitude  $5 \mu\text{m}$  away from the bubble interface at  $\theta = 33^\circ$  where the maximum velocity is found according to Fig. 9. Time is plotted on a logarithmic scale.

to the simulation methodology applied and moderates the possible influence of bubble growth. Besides, it can be stated that the influence of thermal buoyancy, as taken into account also in the simulations according to eq. (5), is of minor importance only with respect to the Marangoni convection near the attached hydrogen bubble. Although not shown, additional simulations performed when neglecting buoyancy were found to deliver almost identical results, as the buoyant convection is much weaker than the Marangoni convection. A characteristic ratio of both types of convection can be estimated by calculating the ratio of Grashof to Reynolds number squared [45]. When using the bubble radius as characteristic length scale, with the maximum values of the temperature difference  $\Delta T$  and the Marangoni velocity  $U$  found in the simulation, it amounts to about  $Gr/Re^2 = \beta g R \Delta T / U^2 \sim 0.07$  only.

Furthermore, in the simulations, the convection inside the hydrogen bubble and thus the convective transport of heat was neglected. However, the recirculating flow driven in the gas bubble but neglected here is unlikely to cause the difference observed. As mentioned above, diffusion of heat dominates compared to the advective transport of heat in the bubble. Fig. 10 shows an additional curve (light blue line) of the shear stress calculated from numerical temperature data obtained when the thermal diffusivity of hydrogen is artificially enhanced by a factor of 10. The close match with the experimentally obtained shear stress from temperature data clearly supports this reasoning.

Due to lack of data, in the simulations, the surface tension data ( $\sigma_0, \gamma_1$ ) from the material combination water/air were used instead of electrolyte/hydrogen, which is justified by the following reasoning. The high surface tension of water is the result of strong cohesive forces between the water molecules due to the formation of hydrogen bonds. Therefore, the surface tension of water is only marginally affected by a change in the gas atmosphere from air to hydrogen since the interaction between the gas and water molecules is very weak. The sulfate anions in the present electrolyte also undergo hydrogen bondings with the water molecules, thereby increasing the surface tension by about 1-2 %, depending on concentration. However, for a bubble of given shape, a modification of the value of the surface tension itself ( $\sigma_0$ ) does not alter the Marangoni convection at all. The effect is determined by the value of the temperature coefficient  $\gamma_1$  only. Despite water/hydrogen data were not available, the argumentation above suggests that it is quite reasonable to assume that the value for water/air is valid, as also the temperature-dependent equilibrium of water evaporation should be about the same.

Additionally, as it is known that the Henry coefficient depends on temperature, neglected solutal Marangoni effects are estimated. The saturation concentration of dissolved hydrogen at temperature  $T$  can be determined from [46]

$$c_{\text{sat}}(T) = c_{\text{sat}}(T_{\text{ref}}) \cdot \exp \left[ 500 \text{ K} \left( \frac{1}{T} - \frac{1}{T_{\text{ref}}} \right) \right].$$

If the temperature would rise by 50 K, the saturation concentration would reduce by about 0.17 mol/m<sup>3</sup>. The coefficient of solutal H<sub>2</sub> variation of the surface tension is  $\gamma_2^{\text{H}_2} = -3.2 \cdot 10^5 \text{ Nm}^2/\text{mol}$ . Thus, the temperature rise would increase the surface tension by about 5  $\mu\text{N/m}$ . In comparison, by using the thermocapillary coefficient of dissolved hydrogen of  $\gamma_1 = -1.6 \cdot 10^{-4} \text{ N}/(\text{m} \cdot \text{K})$ , a temperature rise by 50 K directly reduces the surface tension by about 8 mN/m. Thus, the temperature dependence of the Henry constant can be safely ignored, as the related changes of surface tension are at least 1000 times smaller than the thermocapillary effect. Besides, as the temperature is re-

produced nicely in the simulation, temperature-related effects are unlikely to improve the match between experiment and simulation.

Further solutal Marangoni effects might arise from the possible depletion of the electrolyte of  $\text{H}_2\text{SO}_4$  near the microelectrode. The current density in the wedge at the configuration studied here amounts to about  $10^7 \text{ A/m}^2$ , at which the pH of the electrolyte can be expected to increase [47], and water splitting is likely to contribute to the mass transfer at the cathode. When neglecting electromigration effects, the diffusive length scale over which  $\text{H}_2\text{SO}_4$  depletion occurs can be estimated from  $L \sim \sqrt{D_{\text{H}_2\text{SO}_4} \cdot \tau_b}$  where  $D_{\text{H}_2\text{SO}_4} \sim 3 \cdot 10^{-9} \text{ m}^2/\text{s}$  and  $\tau_b \sim 4.1 \text{ s}$  denote the coefficient of molecular diffusion of  $\text{H}_2\text{SO}_4$  and the bubble cycle, respectively. Thus, a length of only about  $111 \mu\text{m}$  is obtained. However, thermocapillary convection will at the same time replenish fresh electrolyte in the wedge and advect depleted electrolyte along the interface. As this effect in the wedge where convection is slow is difficult to quantify, the numerical simulations were extended by considering additionally a convection-diffusion equation for the concentration  $c$  of  $\text{H}_2\text{SO}_4$ :

$$\frac{\partial c}{\partial t} + \vec{u} \cdot \nabla T = D_{\text{H}_2\text{SO}_4} \Delta c \quad (9)$$

The boundary conditions applied are complete depletion at the cathode whereas at other boundaries species flux has to vanish. From the result of the simulation shown in Fig. 12 it is to be seen that the concentration gradient builds up quickly within less than a second and does not change significantly at longer times. Most importantly, only small changes of concentration at angles  $\theta \geq 15^\circ$  appear.

Thus, the local depletion of the electrolyte near the microelectrode is unlikely to cause the differences in convection found only at larger angles of  $\theta > 35^\circ$ . Similar arguments apply for possible electromigration effects neglected so far. Those are expected to play a role only close to the microelectrode where the electric field is strong but are unlikely to be the reason for the mismatch of velocity and stress more far away from the microelectrode.

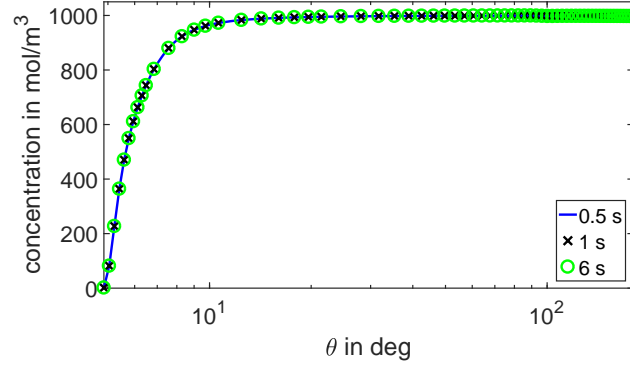


Figure 12: Concentration of  $\text{H}_2\text{SO}_4$  along the interface versus angle  $\theta$  (logarithmic scaling) at different instants of time  $t$ .

Finally, additional temperature effects due to larger Ohmic losses in the depleted volume and related buoyancy effects occur but are expected to be negligible, as the maximum values of temperature and velocity of experiment and simulation nicely match. This also indicates that the approximate use of the primary current distribution in the simulations is reasonable, as the main specifics of the problem arise from the drastic increase of the current density near the wetted part of the microelectrode, thereby reaching values of about  $10^6 \text{ A/m}^2$  at the cathode, and the related strong local heating ( $\sim j^2$ ). Possible differences between experiment and simulation using the primary current density could be caused by the reaction overpotential, the related energy of which is partially lost for heating, and by spatial variation of the electrical conductivity. However, based on an extrapolation from data published by [48], the overpotential at the platinum cathode at the current density mentioned above can be estimated to about 0.15 V, which is about two percent of the cathodic potential only. Additionally, those local losses of heating power might be counterbalanced by a smaller electrical conductivity of the depleted electrolyte near the cathode, as mentioned above, which is also not considered when using the primary current density. In summary, using the primary current density is supported by these estimations, which, of course, should be validated by improved simulation models in the future.

Last, the possible influence of electrocapillarity is discussed, which, as mentioned in the introduction, arises from the dependence of the surface tension on the electric potential at the interface,

and is not taken into account in the simulation. It should be pointed out here that this effect is equivalent to considering Maxwell stress boundary conditions with a known surface charge density at the interface, as defined in the Taylor Melcher leaky dielectric model [49, 50]. From earlier analytical work it is known that the Maxwell stress arising at the interface of a gas bubble and a conductive medium in a vertical electrical field will cause upward interfacial convection below the equator and downward interfacial convection above it, thus leading to a double vortex flow in the meridional plane [51]. Despite in our case the geometry and the electric field distribution are more complex, as the bubble is attached at a microelectrode, it could be speculated that a qualitatively similar shear pattern would be caused. Then, the electrocapillary effect might be too weak to become visible below the equator where the thermocapillary effect dominates, but it might prevail above the equator where the thermocapillary effect is much weaker to trigger the departure of the interfacial flow, as seen in the experiment. Thus, it could also contribute to an improved match of both the velocity stress along the interface and the center position of the recirculating flow. However, evidence has to be left to future investigations.

In conclusion, the convection found in the hydrogen evolution electrolysis experiments at microelectrodes can largely be attributed to the thermocapillary effect caused by Ohmic heating due to the high current density appearing at the microelectrode. Numerical simulation proves that main features of the convection forced parallel to the interface near the microelectrode and also the related temperature distribution can be attributed to the thermal Marangoni effect. Further research might be necessary to resolve the origin of the small differences found between simulation and experiment. The discussion above tends to rule out solutal effects whereas electrocapillary effects are likely to play a role.

- [1] X. Yang, D. Baczyzmalski, C. Cierpka, G. Mutschke, K. Eckert, Marangoni convection at electrogenerated hydrogen bubbles, *Physical Chemistry Chemical Physics* 20 (2018) 11542–11548.
- [2] F. Karnbach, X. Yang, G. Mutschke, J. Fröhlich, J. Eckert, A. Gebert, K. Tschulik, K. Eckert, M. Uhlemann, Interplay of the open circuit potential-relaxation and the dissolution behavior of a single  $H_2$  bubble generated at a  $\mu$ pt microelectrode, *The Journal of Physical Chemistry C* 120 (2016) 15137–15146.
- [3] D. Pletcher, X. Li, Prospects for alkaline zero gap water electrolyzers for hydrogen production, *International Journal of Hydrogen Energy* 36 (2011) 15089–15104.
- [4] N. Nagai, M. Takeuchi, T. Kimura, T. Oka, Existence of optimum space between electrodes on hydrogen production by water electrolysis, *International Journal of Hydrogen Energy* 28 (2003) 35–41.
- [5] H. Vogt, R. Balzer, The bubble coverage of gas-evolving electrodes in stagnant electrolytes, *Electrochimica Acta* 50 (2005) 2073–2079.
- [6] M. Wang, Z. Wang, X. Gong, Z. Guo, The intensification technologies to water electrolysis for hydrogen production—a review, *Renewable and Sustainable Energy Reviews* 29 (2014) 573–588.
- [7] T. Iida, H. Matsushima, Y. Fukunaka, Water electrolysis under a magnetic field, *Journal of The Electrochemical Society* 154 (2007) E112–E115.
- [8] H. Matsushima, D. Kiuchi, Y. Fukunaka, Measurement of dissolved hydrogen supersaturation during water electrolysis in a magnetic field, *Electrochimica Acta* 54 (2009) 5858–5862.
- [9] H. Matsushima, T. Iida, Y. Yasuhiro Fukunaka, Gas bubble evolution on transparent electrode during water electrolysis in a magnetic field, *Electrochimica Acta* 100 (2013) 261–264.
- [10] D. Baczyzmalski, T. Weier, C. J. Kähler, C. Cierpka, Near-wall measurements of the bubble-and lorentz-force-driven convection at gas-evolving electrodes, *Experiments in Fluids* 56 (2015) 162.
- [11] H. Liu, L. Pan, H. Huang, Q. Qin, P. Li, J. Wen, Hydrogen bubble growth at micro-electrode under magnetic field, *Journal of Electroanalytical Chemistry* 754 (2015) 22 – 29.
- [12] D. Baczyzmalski, F. Karnbach, X. Yang, G. Mutschke, M. Uhlemann, K. Eckert, C. Cierpka, On the electrolyte convection around a hydrogen bubble evolving at a microelectrode under the influence of a magnetic field, *Journal of The Electrochemical Society* 163 (2016) E248–E257.
- [13] D. Baczyzmalski, F. Karnbach, G. Mutschke, X. Yang, K. Eckert, M. Uhlemann, C. Cierpka, Growth and detachment of single hydrogen bubbles in a magnetohydrodynamic shear flow, *Physical Review Fluids* 2 (2017) 093701.
- [14] G. Mutschke, D. Baczyzmalski, C. Cierpka, K. Karnbach, M. Uhlemann, X. Yang, K. Eckert, J. Fröhlich, Numerical simulation of mass transfer and convection near a hydrogen bubble during water electrolysis in a

- magnetic field, *Magnetohydrodynamics* 1 (2017) 193–199.
- [15] T. Weier, D. Baczyzmalski, J. Massing, S. Landgraf, C. Cierpka, The effect of a lorentz-force-driven rotating flow on the detachment of gas bubbles from the electrode surface, *International Journal of Hydrogen Energy* 42 (2017) 20923–20933.
  - [16] D. Matsushima, H. and Kiuchi, Y. Fukunaka, K. Kuribayashi, Single bubble growth during water electrolysis under microgravity, *Electrochemistry Communications* 11 (2009) 1721–1723.
  - [17] H. Matsushima, Y. Fukunaka, K. Kuribayashi, Water electrolysis under microgravity Part II. Description of gas bubble evolution phenomena, *Electrochimica Acta* 51 (2006) 4190–4198.
  - [18] D. Fernández, M. Martine, A. Meagher, M. E. Möbius, J. Coey, Stabilizing effect of a magnetic field on a gas bubble produced at a microelectrode, *Electrochemistry Communications* 18 (2012) 28–32.
  - [19] D. Fernández, P. Maurer, M. Martine, J. Coey, M. E. Möbius, Bubble formation at a gas-evolving microelectrode, *Langmuir* 30 (2014) 13065–13074.
  - [20] L. Luo, H. S. White, Electrogeneration of single nanobubbles at sub-50-nm-radius platinum nanodisk electrodes, *Langmuir* 29 (2013) 11169–11175.
  - [21] X. Yang, F. Karnbach, M. Uhlemann, S. Odenbach, K. Eckert, Dynamics of single hydrogen bubbles at a platinum microelectrode, *Langmuir* 31 (2015) 8184–8193.
  - [22] R. T. Perera, C. E. Arcadia, J. Rosenstein, Probing the nucleation, growth, and evolution of hydrogen nanobubbles at single catalytic sites, *Electrochimica Acta* 283 (2018) 1773–1778.
  - [23] H. Vogt, On the supersaturation of gas in the concentration boundary layer of gas evolving electrodes, *Electrochimica Acta* 25 (5) (1980) 527 – 531.
  - [24] C. Marangoni, On the expansion of a droplet of a liquid floating on the surface of another liquid, *Tipografia dei fratelli Fusi, Pavia*, 1865.
  - [25] J. Chen, L. Guo, X. Hu, Z. Cao, Y. Wang, Dynamics of single bubble departure from TiO<sub>2</sub> nanorod-array photoelectrode, *Electrochimica Acta* 274 (2018) 57–66.
  - [26] R. F. Engberg, M. Wegener, E. Y. Kenig, The impact of Marangoni convection on fluid dynamics and mass transfer at deformable single rising droplets—A numerical study, *Chemical Engineering Science* 116 (2014) 208–222.
  - [27] M. Wegener, A numerical parameter study on the impact of marangoni convection on the mass transfer at buoyancy-driven single droplets, *International Journal of Heat and Mass Transfer* 71 (2014) 769–778.
  - [28] J. Chen, C. Yang, Z.-S. Mao, The interphase mass transfer in liquid–liquid systems with marangoni effect, *The European Physical Journal Special Topics* 224 (2015) 389–399.



- [29] J. Straub, The role of surface tension for two-phase heat and mass transfer in the absence of gravity, *Experimental Thermal and Fluid Science* 9 (1994) 253–273.
- [30] S. Petrovic, T. Robinson, R. L. Judd, Marangoni heat transfer in subcooled nucleate pool boiling, *International Journal of Heat and Mass Transfer* 47 (2004) 5115–5128.
- [31] V. K. Dhir, G. R. Warrier, E. Aktinöl, D. Chao, J. Eggers, W. Sheredy, W. Booth, Nucleate pool boiling experiments (NPBX) on the International Space Station, *Microgravity Science and Technology* 24 (2012) 307–325.
- [32] H. H. Bauer, Theory of polarographic maxima of the first kind, *Electrochimica Acta* 18 (1973) 427–431.
- [33] S. Lubetkin, The motion of electrolytic gas bubbles near electrodes, *Electrochimica Acta* 48 (2002) 357–375.
- [34] H.-J. Butt, K. Graf, M. Kappl, *Physics and Chemistry of Interfaces*, Wiley-VCH Verlag & Co. KGaA, 2003.
- [35] B. J. Kirby, *Micro- and Nanoscale Fluid Mechanics*, Cambridge University Press, 2010.
- [36] J. Massing, D. Kaden, C. J. Kähler, C. Cierpka, Luminescent two-color tracer particles for simultaneous velocity and temperature measurements in microfluidics, *Measurement Science and Technology* 27 (2016) 015301.
- [37] J. Sakakibara, R. Adrian, Measurement of temperature field of a Rayleigh-Bénard convection using two-color laser-induced fluorescence, *Experiments in Fluids* 37 (2004) 331–340.
- [38] S. Someya, Y. Li, K. Ishii, K. Okamoto, Combined two-dimensional velocity and temperature measurements of natural convection using a high-speed camera and temperature-sensitive particles, *Experiments in Fluids* 50 (2011) 65–73.
- [39] J. Massing, C. J. Kähler, C. Cierpka, A volumetric temperature and velocity measurement technique for microfluidics based on luminescence lifetime imaging, *Experiments in Fluids* 59 (2018) 163.
- [40] Q. Zhou, N. Erkan, K. Okamoto, Ex situ calibration technique for simultaneous velocity and temperature measurements inside water droplets using temperature-sensitive particles, *Measurement Science and Technology* 28 (2017) 075203.
- [41] C. Cierpka, B. Lütke, C. J. Kähler, Higher order multi-frame Particle Tracking Velocimetry, *Experiments in Fluids* 54 (2013) 1533.
- [42] H. Verhaart, R. De Jonge, S. Van Stralen, Growth rate of a gas bubble during electrolysis in supersaturated liquid, *International Journal of Heat and Mass Transfer* 23 (1980) 293–299.
- [43] C. J. Kähler, S. Scharnowski, C. Cierpka, On the uncertainty of digital PIV and PTV near walls, *Experiments in Fluids* 52 (2012) 1641 – 1656.
- [44] R. Clift, J. R. Grace, M. E. Weber, *Bubbles, drops, and particles*, Courier Corporation, 2005.
- [45] A. Bejan, *Convection heat transfer*, John Wiley & Sons, 2013.
- [46] R. Sander, *Compilation of Henry’s law constants (version 4.0) for water as solvent.*, Atmospheric Chemistry and

Physics 15 (8).

- [47] A. Kuhn, C. Chan, pH changes at near-electrode surfaces, *Journal of Applied Electrochemistry* 13 (1983) 189–207.
- [48] S. Schuldiner, Hydrogen overvoltage on bright platinum, *J. Electrochem. Soc.* 99 (1952) 488–494.
- [49] J. Baygents, D. Saville, Electrophoresis of drops and bubbles., *Journal of the Chemical Society Faraday Transactions* 87 (1991) 1883–1898.
- [50] D. Johnson, Electrocapillary flows, *Lecture Notes in Physics* 628 (2003) 291–304.
- [51] J. Melcher, G. Taylor, Electrohydrodynamics: A review of the role of interfacial shear stresses., *Annual Review of Fluid Mechanics* 1 (1969) 111–146.